

[COR: alpha]

Memristor-coupled asymmetric neural networks: bionic modeling, chaotic dynamics analysis and encryption application

Hairong Lin^a, Chunhua Wang^a, Jingru Sun^{a,*}, Xin Zhang^b, Yichuang Sun^c and Herbert H. C. Iu^d

^aCollege of Computer Science and Electronic Engineering, Hunan University, Changsha 410082, China

^bCollege of Electrical and Information Engineering, Hunan University, Changsha 410082, China

^cSchool of Engineering and Computer Science, University of Hertfordshire, Hatfield AL10 9AB, U.K

^dSchool of Electrical, Electronic and Computer Engineering, University of Western Australia, Perth, WA 6009, Australia

ARTICLE INFO

Keywords:

Asymmetric neural network
Chaotic dynamics
Memristor
Image encryption
Circuit implementation

ABSTRACT

With the rapid development of artificial intelligence, it has important theoretical and practical significance to construct neural network models and study their dynamical behaviors. This article mainly focuses on the bionic model and chaotic dynamics of the asymmetric neural network as well as its engineering application. We first construct a memristor-coupled asymmetric neural network (MANN) utilizing two asymmetrical sub-neural networks and a coupled multipiecewise memristor synapse. Then, the chaotic dynamics of the proposed MANN is studied and analyzed by using basic dynamics methods like equilibrium stability, bifurcation diagrams, Lyapunov exponents, and Poincare mappings. Research results show that the proposed MANN exhibits multiple complex dynamical characteristics including infinitely wide hyperchaos with amplitude control, hyperchaotic initial-boosted behavior, and arbitrary number of hyperchaotic multi-structure attractors. More importantly, the phenomena of the infinitely wide hyperchaos and the hyperchaotic multi-structure attractors are observed in neural networks for the first time. Meanwhile, applying the hyperchaotic multi-structure attractors, a color image encryption scheme is designed based on the proposed MANN. Performance analyses show that the designed encryption scheme has some merits in correlation, information entropy, and key sensitivity. Finally, a physical circuit of the MANN is implemented and various typical dynamical behaviors are verified by hardware experiments.

1. Introduction

The human brain which exhibits many special dynamics is considered an extremely complex dynamical system [1]. In order to research brain dynamics, various neural network models have been established by emulating the biological structure and working mechanism of the brain [2], [3]. Among these models, Hopfield neural network (HNN) is commonly used as a typical paradigm due to its particular network structure and abundant brain-like chaotic dynamics [4]. Over the past decades, chaotic dynamics based on the HNNs has been extensively studied by researchers from various perspectives.

In the early days, the study on the chaotic dynamics of the HNNs mainly focused on the original HNN models with few neurons. For example, various dynamical behaviors like chaos [5], hyperchaos [6], chaotic bursting firings [7], and coexisting attractors [8] have been found in some original HNNs with two, three, or four neurons. Since the memristor was found in 2008 [9], the memristive HNNs have attracted much attention in the investigation of chaotic dynamics. The memristor is a novel nonlinear circuit component, which owns the special property of memory function [10,11] and chaotic characteristic [12,13]. Therefore, a mass of memristive HNNs have been constructed by employing memristor to simulate biological neural synapses [14–16]. Due to the introduction of memristor synapses, memristive HNNs can generate complex dynamical behaviors closer to brain dynamics. For instance, utilizing a linear memristor as a synapse in an HNN with two neurons can make memristive HNN exhibit complex multistability [17]. With a multi-stable memristor synapse introduced into an HNN with four neurons, extreme multistability was discovered in a memristive

*Corresponding author

 jt_sunjr@hnu.edu.cn (J. Sun)

ORCID(s):

HNN [18]. Hidden extreme multistability was found in a memristive HNN by introducing a hyperbolic memristor synapse into the HNN [19]. Moreover, complicated multi-scroll attractors were detected from a memristive HNN with a multi-piecewise memristor synapse [20]. In particular, a recent study showed that a memristive symmetric neural network with two sub-neural networks can generate complex brain-like hyperchaotic initial-boosted behavior [21]. This means that the coupled neural networks have complex dynamical behaviors closer to the brain. Also, some results show that the memristive neurons and memristive neural networks exhibit more complex collective dynamics [22–24]. Meanwhile, the circuits of memristive neural networks show higher efficiency and lower power due to the use of real nano-memristor devices [25, 26].

On the other hand, more and more researchers focus on the application of the HNNs in various artificial intelligence fields such as machine learning [27], image recognition [28], and information security [29]. In particular, the application of chaotic signals generated by the HNNs to image encryption has attracted increasing attention from many researchers. Chaotic signals with inherent randomness and ergodicity can be applied to generate pseudo-random numbers [30–32]. Many studies have shown excellent encryption performances in image encryption algorithms based on the HNNs with complex chaotic behaviors. For example, using a hyperchaotic HNN to generate a keystream, a robust hybrid image encryption algorithm was designed [33]. By utilizing chaotic HNNs to generate diffusion matrixes, some color image encryption algorithms were proposed [34–36]. Furthermore, a medical image encryption scheme was realized, in which a multi-stable HNN is used to produce the key [37]. Recently, several image encryption schemes based on memristive HNNs with multi-scroll attractors or initial-boosted behavior have been presented [20, 21, 38]. Due to their complex dynamical behaviors, these encryption schemes show better security performances than previous schemes.

From the above review, it becomes clear that three issues still need further consideration. Firstly, the existing studies mainly focus on the neural networks or symmetric neural networks. In fact, the real biological neural systems are asymmetrical [39]. Although there are some findings on the dynamics of asymmetric neural networks [40–42], the chaotic dynamics of the asymmetric neural networks has not been studied in depth. Thus, the study on chaotic dynamics of the asymmetric neural networks is significant and valuable. Secondly, the previous **researches** of the HNNs mainly **focus** on one of the dynamical characteristics such as hyperchaotic behavior, multi-scroll behavior, coexisting behavior, or initial-boosted behavior. The phenomenon of multiple dynamical behaviors simultaneously generated by a neural network has not been explored. **The brain's nervous system can exhibit multiple dynamical behaviors such as resting state, spiking firing, bursting firing, and chaos, which has the features of multistability [43]. There is no doubt that compared with neural network models without multistability, neural networks with multistability are closer to the real nervous system.** Therefore, concurrently generating multiple dynamical behaviors through a neural network is worthy of in-depth study. Finally, many existing dynamical phenomena like chaotic and hyperchaotic attractors, coexisting attractors, and multi-scroll attractors have been found and applied in different HNNs. However, hyperchaotic multi-structure attractors have not been reported in HNNs. More importantly, compared with the existing dynamical behaviors, the hyperchaotic multi-structure attractors may have more complex dynamical characteristics, and the complex dynamics come from the fact that the brain is a high-order complex dynamical system [44]. The higher complexity of dynamical behaviors, the greater the randomness of chaotic signals, resulting in better security when the hyperchaotic multi-structure attractors are used in information encryption. Hence it is greatly significant to explore chaotic phenomena from high-order neural network models.

Motivated by the above analyses, this article researches the chaotic dynamics of the asymmetric neural network and its application in image encryption. To the best of our knowledge, this is the first time that the chaotic dynamical behaviors of the asymmetric neural networks are investigated. The main novelty and contributions of this study are summarized as follows:

- 1) A novel bionic MANN model for exploring chaotic dynamics is constructed. Unlike the previous models in [17–21], this model is modeled by using two asymmetric sub-neural networks to emulate two different encephalic regions.

- 2) Multiple chaotic phenomena including infinitely wide hyperchaos with amplitude control, hyperchaotic initial-boosted behavior, and hyperchaotic multi-structure attractors are obtained from the proposed MANN.

- 3) Based on the hyperchaotic multi-structure attractors, a novel color image encryption scheme is presented. Compared with similar schemes in [33–36, 46], the proposed encryption scheme has lower correlation, higher information entropy, and higher key sensitivity.

- 4) Last but not least, an analog neural network circuit is implemented and hardware experiment is performed to verify the observed chaotic dynamics including various chaotic attractors.

The rest of the article is organized as follows. Section 2 describes the modeling process of the MANN. Section 3 reveals the chaotic dynamics of the proposed MANN. A chaos-based image encryption scheme is designed in Section 4. Section 5 presents the circuit implementation. Section 6 summarizes the article.

2. MANN model description

This section first designs two sub-neural networks then introduces a flux-controlled multi-piecewise memristor, and finally constructs a memristor-coupled asymmetric neural network model.

2.1 Design of sub-neural networks

HNN with brain-like network structure and rich chaotic dynamics is regarded as an ideal brain neural network model [7, 8]. An original HNN with n neurons can be represented by [4]

$$C_i \dot{v}_i = -\frac{v_i}{R_i} + \sum_{j=1}^n w_{ij} \tanh(v_j) + I_i \quad (i, j \in N^*) \quad (1)$$

where v_i , C_i and R_i are the membrane potential, capacitance and resistance of neuron i , respectively. w_{ij} and I_i are the synaptic weight coefficient and external bias current, respectively. Additionally, $\tanh(\cdot)$ is the neuron activation function. It follows that different sub-neural network models can be designed by selecting different number of neurons and suitable synaptic weight coefficients. Here, one sub-neural network with four neurons and another sub-neural network with three neurons are proposed by adopting the trial and error method. Let $C_i=1$, $R_i=1$, $I_i=0$ ($i=1, 2, 3, 4$), the proposed two asymmetric sub-neural networks can be respectively expressed as follows

$$\begin{cases} \dot{x}_1 = -x_1 + 1.8 \tanh(x_1) + 3.4 \tanh(x_2) - 0.5 \tanh(x_3) - 12 \tanh(x_4) \\ \dot{x}_2 = -x_2 + \tanh(x_2) + 20 \tanh(x_3) - 0.5 \tanh(x_4) \\ \dot{x}_3 = -x_3 + 0.5 \tanh(x_1) - 4 \tanh(x_2) + 1.8 \tanh(x_3) + 4 \tanh(x_4) \\ \dot{x}_4 = -x_4 + 0.82 \tanh(x_1) + 0.5 \tanh(x_3) + 2 \tanh(x_4) \end{cases} \quad (2)$$

$$\begin{cases} \dot{y}_1 = -y_1 + 0.1 \tanh(y_1) + 0.5 \tanh(y_2) - 2.5 \tanh(y_3) \\ \dot{y}_2 = -y_2 + 3 \tanh(y_2) + 3 \tanh(y_3) \\ \dot{y}_3 = -y_3 + \tanh(y_1) - 3 \tanh(y_2) + \tanh(y_3) \end{cases} \quad (3)$$

where x_i and y_i denote the membrane potentials of neurons X_i and Y_i , respectively.

2.2 Introduction of memristor synapse

Memristors have been widely applied to emulate neural synapses because of their synapse-like adjustability and memory [45]. Recently, Lin et al presented a flux-control multi-piecewise memristor model [46], and it is described as

$$\begin{cases} i = W(\varphi)v = (a + b\varphi)v \\ d\varphi/dt = cv - dh(\varphi) \end{cases} \quad (4)$$

where a , b , c and d are four memristor parameters. φ represents the inner state variables and $W(\varphi)$ denotes the memductance function. The internal state variable function $h(\varphi)$ can be written as

$$h(\varphi) = \begin{cases} h_1(\varphi) = \begin{cases} \varphi, N = 0 \\ \varphi - \sum_{i=1}^N (\text{sgn}(\varphi + (2i - 1)) + \text{sgn}(\varphi - (2i - 1))) \\ N = 1, 2, 3, \dots \end{cases} \\ h_2(\varphi) = \begin{cases} \varphi - \text{sgn}(\varphi), M = 0 \\ \varphi - \text{sgn}(\varphi) - \sum_{j=1}^M (\text{sgn}(\varphi + 2j) + \text{sgn}(\varphi - 2j)) \\ M = 1, 2, 3, \dots \end{cases} \end{cases} \quad (5)$$

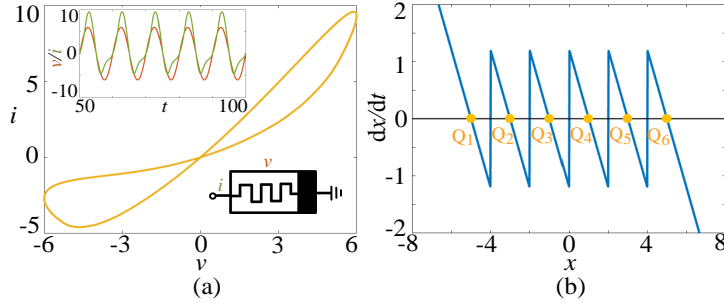


Figure 1: The unique performance of the multi-pieewise memristor model. (a) v - i characteristics. (b) POP curve.

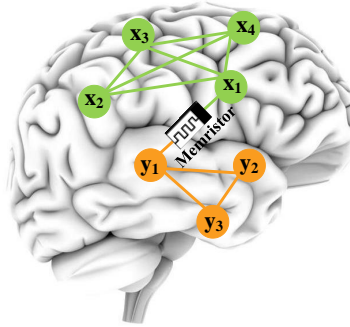


Figure 2: Concept diagram of the MANN model.

where N and M are memristor control parameters. Note that the internal state variable function $h(\varphi)$ can be changed by selecting different values of N and M in $h_1(\varphi)$ and $h_2(\varphi)$, respectively. When a sinusoidal voltage $v=6\sin(2\pi0.1t)$ with $a=1$, $b=0.05$, $c=2.2$, $d=1.2$, $M=2$, is applied in the memristor, it can exhibit pinched hysteresis loop on the v - i plane, as shown in Fig.1(a). The memristors can be used to simulate neural synapses due to their memory characteristic [47]. The power-off plot (POP) curve provides a method to check the non-volatile memory of a memristor [48]. By solving (4) with $v=0$, one can plot the curve of POP, as shown in Fig.1(b). According to the non-volatile memristor theorem [49], a memristor is non-volatile if its POP intersects the x -axis at 2 or more points with a negative slope. From Fig.1(b), there are 6 intersection points (Q_1 - Q_6) with a negative slope. Thus, the multi-pieewise memristor has the characteristic of non-volatile memory. More importantly, further study shows that the number of intersection points with a negative slope is equal to $2M+2$ or $2N+1$. Therefore, the multi-pieewise memristor has a very strong ability of non-volatile memory, which means that it is very suitable for emulating neural synapses.

2.3 Construction of MANN

The human brain contains multiple encephalic regions with different neurological functions [44]. However, these encephalic regions are not independent. On the contrary, there are strong connections between them and the functional connectivity between different regions shows complex neural dynamics. For instance, the ability of thought is collectively influenced by the frontal lobe and the parietal lobe in the brain [50]. Furthermore, the visual impairment and memory deficiency will occur synchronously, when the occipital lobe is damaged [51]. Undoubtedly, the research on the dynamical behavior of the coupled neural networks with two different sub-neural networks, namely encephalic regions, is significant and valuable [40, 41]. It is well known that the neural signal can be exchanged between neurons and neural networks through neural synapses [10]. Many research results show that the memristor can be used to emulate the functions of biological neural synapses [11, 17, 18]. Here, using the presented multi-pieewise memristor to emulate the coupling synapse between the proposed two asymmetric sub-neural networks. As shown in Fig.2, a MANN model is constructed, where the two different sub-neural networks stand for two different encephalic regions in the brain. When a membrane potential difference occurs between two coupled neurons, a magnetic induction current will be generated [21]. The magnetic induction current can be described by the flux-controlled multi-pieewise

memristor. Consequently, a mathematical model of the MANN is given as follows

$$\begin{cases} \dot{x}_1 = -x_1 + 1.8 \tanh(x_1) + 3.4 \tanh(x_2) - 0.5 \tanh(x_3) - 12 \tanh(x_4) - \mu W(\varphi)(x_1 - y_1) \\ \dot{x}_2 = -x_2 + \tanh(x_2) + 20 \tanh(x_3) - 0.5 \tanh(x_4) \\ \dot{x}_3 = -x_3 + 0.5 \tanh(x_1) - 4 \tanh(x_2) + 1.8 \tanh(x_3) + 4 \tanh(x_4) \\ \dot{x}_4 = -x_4 + 0.82 \tanh(x_1) + 0.5 \tanh(x_3) + 2 \tanh(x_4) \\ \dot{y}_1 = -y_1 + 0.1 \tanh(y_1) + 0.5 \tanh(y_2) - 2.5 \tanh(y_3) + \mu W(\varphi)(x_1 - y_1) \\ \dot{y}_2 = -y_2 + 3 \tanh(y_2) + 3 \tanh(y_3) \\ \dot{y}_3 = -y_3 + \tanh(y_1) - 3 \tanh(y_2) + \tanh(y_3) \\ \dot{\varphi} = c(x_1 - y_1) - dh(\varphi) \end{cases} \quad (6)$$

where the additive term $\mu W(\varphi)(x_1 - y_1)$ represents the magnetic induction current induced by the membrane potential difference. The parameter μ denotes the coupling strength of the memristor synapse. The term $-dh(\varphi)$ is an additional magnetic flux caused by the membrane potential fluctuation. **The biological neural network with a large number of neurons is a complex high-dimensional dynamical system [44]. Compared with previous low-dimensional neural network models [17–21], the proposed MANN is closer to the biological neural network.**

3. Chaotic dynamics analysis

In this section, the dynamical behaviors including infinitely wide hyperchaos with amplitude control, hyperchaotic initial-boosted behavior, and hyperchaotic multi-structure attractors are deeply analyzed and discussed. It should be noted that the complexity discussed in this paper is within the scope of chaotic dynamics. From the perspective of chaotic dynamics, hyperchaos is more complex than chaos [52], the multi-structure attractor is more complex than the single-structure attractor [20], and multistability is more complex than single stability [18].

3.1 Infinitely wide hyperchaos with amplitude control

Hyperchaos with more than two positive Lyapunov exponents widely exists in various nonlinear systems [53], especially complex neural networks [54]. Although hyperchaos has been found in HNNs, they only exist within a certain range of parameters. **Furthermore, amplitude control plays a key role in nonlinear systems and has important applications [55].** However, the hyperchaos with amplitude control has not been reported in previous neural networks. This subsection reveals the interesting phenomenon of infinitely wide hyperchaos with amplitude control in the proposed MANN.

The bifurcation diagrams and Lyapunov exponents are common methods for analyzing the chaotic dynamics of dynamical systems. Let parameters $a=1$, $b=0.01$, $c=2.2$, $d=1.2$, $N=0$, initial states (0.1, 0.1, 0.1, 0.1, 0.1, 0.1, 0.1, 0.1) and use the memristor coupling strength μ as the adjustable parameter. When the μ increases from 0 to 1000, the bifurcation diagram at the maximum value of state variable φ and the corresponding first seven Lyapunov exponents are plotted as shown in Fig.3(a) and Fig.3(b), respectively, where the Lyapunov exponents are calculated adopting Wolf's Jacobian method. From Fig.3, two important phenomena can be observed: (i) the MANN generates hyperchaotic attractors with different amplitudes at the state variable φ with the increase of μ ; (ii) the MANN has a wide range of hyperchaotic oscillation. For example, when $\mu=5$, 100, 500, and 1000, the corresponding hyperchaotic attractors with different amplitudes at φ direction are plotted in Fig.4. In other words, the rescaling of the chaotic attractor is realized by the parameter μ in the proposed MANN. The change of the parameter μ causes the state variables φ to be scaled, which means the change of the parameter μ can control the amplitude of the chaotic attractors. **This special phenomena can emulate neural signals with different amplitudes that represent different dynamical states.** Furthermore, numerous numerical simulations show that the MANN can exhibit hyperchaotic behavior with an infinitely wide parameter range. For example, when $\mu=10^6$, the first eight Lyapunov exponents for the MANN are computed for $t=1E7$ seconds as follows

$$\begin{aligned} L_1 &= 0.1694, L_2 = 0.0773, L_3 = 0, L_4 = -0.5265, \\ L_5 &= -0.6738, L_6 = -0.7451, L_7 = -1.1985, L_8 = -28.6737. \end{aligned} \quad (7)$$

The existence of two positive Lyapunov exponents in (7) makes it clear that the MANN is hyperchaotic. Also, the Kaplan-Yorke dimension of the hyperchaotic neural network is calculated by the following equation

$$D_{KY} = 3 + \frac{LE_1 + LE_2 + LE_3}{|LE_4|} = 3.4686. \quad (8)$$

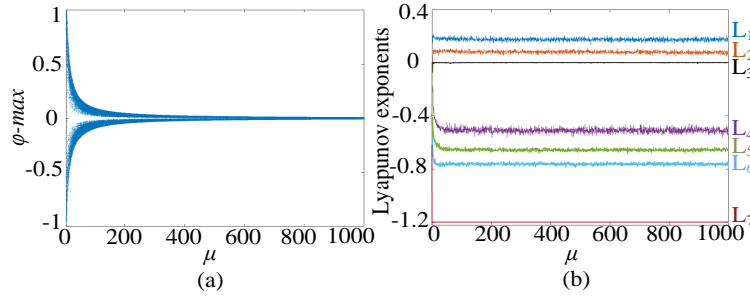


Figure 3: The μ -dependent dynamics with $a=1$, $b=0.01$, $c=2.2$, $d=1.2$, $N=0$. (a) bifurcation diagram. (b) Lyapunov exponents.

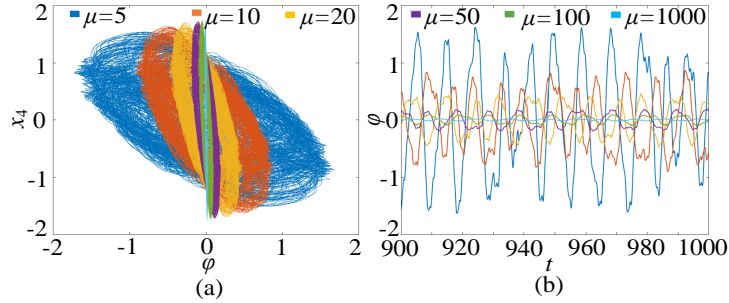


Figure 4: Hyperchaotic attractors with $\mu=5, 10, 20, 50, 100, 1000$. (a) Portrait plots on φ - x_4 plane. (b) Time series of variable φ .

Obviously, the MANN is hyperchaotic since its D_{KY} is a fractal dimension.

3.2 Hyperchaotic initial-boosted behavior

Initial-boosted behavior with coexisting infinitely many attractors with the same topology and different positions is an important dynamical phenomenon and has valuable applications in many engineering fields [56], [57]. It is wonderful that the presented MANN can generate hyperchaotic initial-boosted behavior. For instance, when the parameters a , b , d are kept unchanged, set $c=0.5$, $\mu=8$ and $M=5$, we plot the bifurcation diagram of the φ_0 under initial states $(0.1, 0.1, 0.1, 0.1, 0.1, 0.1, 0.1, \varphi_0)$, as shown in Fig.5(a). As can be seen, the bifurcation diagram displays a typical stair shape, which means that the MANN generate complicated initial-boosted behavior. Meanwhile, the corresponding constant Lyapunov exponents with two positive values in the whole range of the φ_0 variation are given in Fig.5(b). Clearly, the MANN generates hyperchaotic initial-boosted behavior. For example, when set $\varphi_0=\pm 7, \pm 5, \pm 3, \pm 1$, eight coexisting hyperchaotic attractors with the same topologies but different positions can be observed as shown in Fig.6(a). That is to say, the MANN can generate eight hyperchaotic sequences with different positions, as shown in Fig.6(b). Further simulation shows that when continuing to increase the value of M or N , the number of the coexisting hyperchaotic attractors finally tends to infinity. Such phenomenon is very significant because it can provide sustained and robust hyperchaotic sequences and their oscillating amplitudes can be non-destructively adjusted by changing the initial states.

3.3 Hyperchaotic multi-structure attractors

Multi-structure attractors such as multi-scroll/wing attractors have extremely complex dynamics due to their special structure and adjustability [46, 58, 59]. Numerical simulations show that the MANN can generate an arbitrary number of hyperchaotic multi-structure attractors, which has never been reported in existing neural networks. Setting the memristor parameters and initial states as $a=1$, $b=0.01$, $c=2.2$, $d=1.2$, $\mu=8$, $(0.1, 0.1, 0.1, 0.1, 0.1, 0.1, 0.1, 0.1)$, and selecting memristor control parameters N and M as control parameters, the hyperchaotic multi-structure attractors with different number of structures are given in Fig.7. As can be seen from Fig.7, the number of structures generated by the MANN can be controlled by $2N+1$ (odd number) and $2M+2$ (even number). To further reveal its hyperchaotic

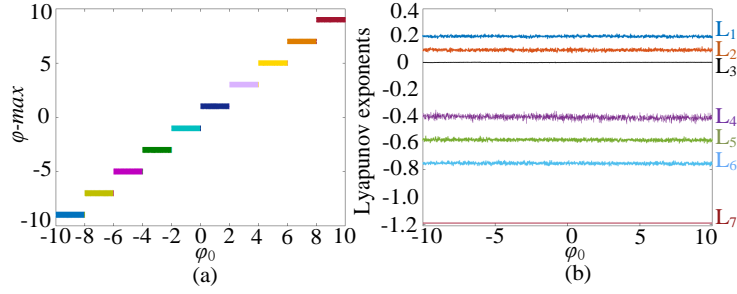


Figure 5: The φ_0 -dependent dynamics with $a=1$, $b=0.01$, $c=0.5$, $d=1.2$, $M=5$. (a) bifurcation diagram. (b) Lyapunov exponents.

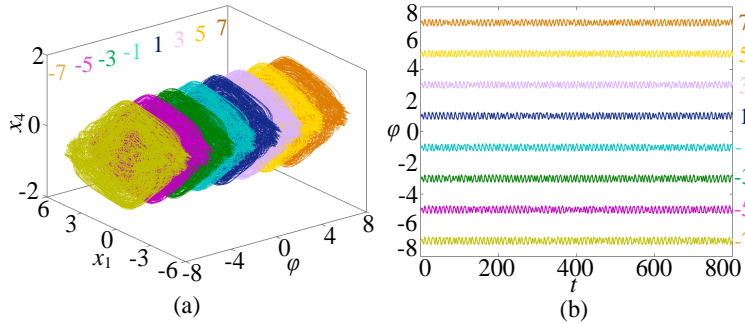


Figure 6: Hyperchaotic initial-boosted behavior with $\varphi_0 = \pm 7, \pm 5, \pm 3, \pm 1$. (a) Portrait plots on φ - x_1 - x_4 space. (b) Time series of variable φ .

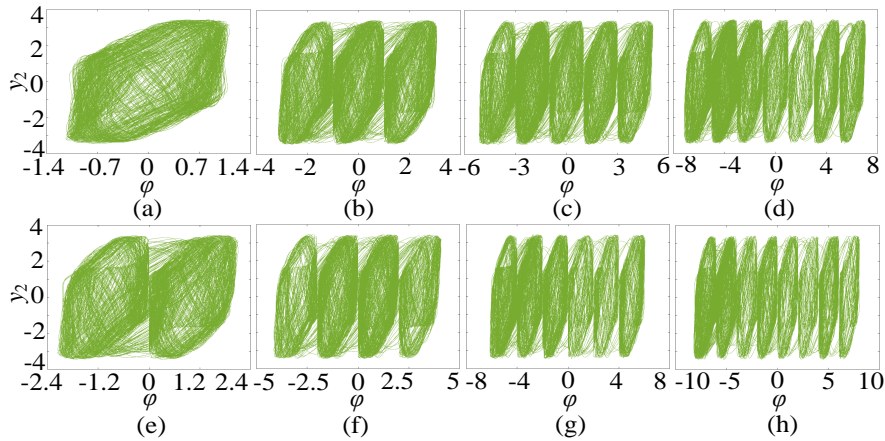


Figure 7: Hyperchaotic n -structure attractors. (a) 1-structure ($N=0$). (b) 3-structure ($N=1$). (c) 5-structure ($N=2$). (d) 7-structure ($N=3$). (e) 2-structure ($M=0$). (f) 4-structure ($M=1$). (g) 6-structure ($M=2$). (h) 8-structure ($M=3$).

characteristic, selecting $M=3$, a bifurcation diagram and corresponding first seven Lyapunov exponents related to parameter $\mu \in (6, 8)$ are shown in Fig.8(a) and Fig.8(b), respectively. From Fig.8, both the bifurcation diagram made up of a dense patch of points and the Lyapunov exponents with two positive values show that the multi-structure attractors are hyperchaotic. In addition, the Poincaré mappings on φ - y_2 and φ - y_1 phase planes for the 8-structure attractor with $x_2=0$ are depicted in Fig.9(a) and Fig.9(b), respectively. Clearly, the Poincaré mappings have the approximate 8-structure maps with irregular shape, implying that the MANN generates extremely complex hyperchaotic behavior.

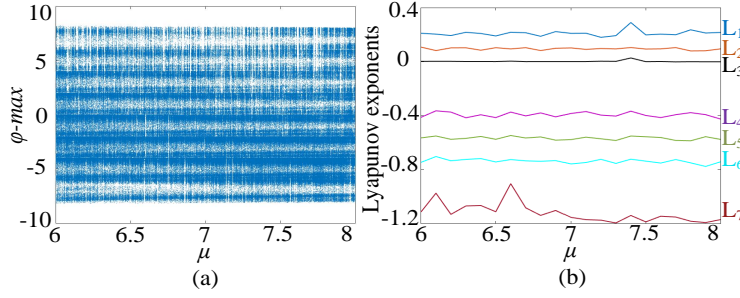


Figure 8: The μ -dependent dynamics with $a=1$, $b=0.01$, $c=2.2$, $d=1.2$, $M=3$. (a) bifurcation diagram. (b) Lyapunov exponents.

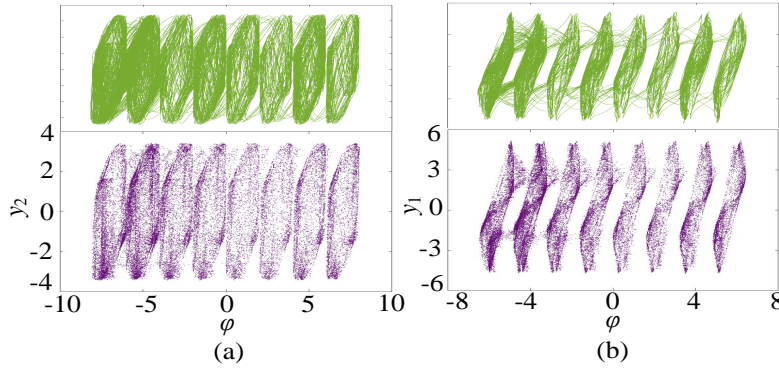


Figure 9: For hyperchaotic 8-structure attractor, phase portraits (top) and Poincaré maps (bottom) with $x_2=0$. (a) φ - y_2 plane. (b) φ - y_1 plane.

The equilibrium points and their stabilities are often used to reveal the generation mechanism of chaotic attractors in dynamic systems. To deeper understanding of the hyperchaotic multi-structure attractors, the equilibrium points and their stabilities are analyzed. Letting the left side of (6) be 0, the equilibrium points of the presented MANN can be calculated by

$$\begin{cases} -x_1 + 1.8 \tanh(x_1) + 3.4 \tanh(x_2) - 0.5 \tanh(x_3) - 12 \tanh(x_4) - \mu W(\varphi)(x_1 - y_1) = 0 \\ -x_2 + \tanh(x_2) + 20 \tanh(x_3) - 0.5 \tanh(x_4) = 0 \\ -x_3 + 0.5 \tanh(x_1) - 4 \tanh(x_2) + 1.8 \tanh(x_3) + 4 \tanh(x_4) = 0 \\ -x_4 + 0.82 \tanh(x_1) + 0.5 \tanh(x_3) + 2 \tanh(x_4) = 0 \\ -y_1 + 0.1 \tanh(y_1) + 0.5 \tanh(y_2) - 2.5 \tanh(y_3) + \mu W(\varphi)(x_1 - y_1) = 0 \\ -y_2 + 3 \tanh(y_2) + 3 \tanh(y_3) = 0 \\ -y_3 + \tanh(y_1) - 3 \tanh(y_2) + \tanh(y_3) = 0 \\ c(x_1 - y_1) - dh(\varphi) = 0 \end{cases} \quad (9)$$

The solution of (9) is solved by using MATLAB numerical method. The results show that there are infinitely discrete equilibrium points that can be written as

$$E = (x_1^*, x_2^*, x_3^*, x_4^*, y_1^*, y_2^*, y_3^*, z^*) = (0, 0, 0, 0, 0, 0, \varphi), h(\varphi) = 0 \quad (10)$$

Evidently, the number of equilibrium points is determined by the internal state variable function $h(\varphi)$. Without loss of generality, we take $M=2$ as an example and keep $a=1$, $b=0.01$, $c=2.2$, $d=1.2$, and $\mu=8$. The equilibrium points at φ - y_2 plane can be drawn as shown in Fig.10, where the red curve denotes the function $h_2(\varphi)$ with $M=2$ and the blue curve represents $y_2=0$. It can be seen from Fig.10 that there are eleven equilibrium points E_1 - E_{11} . Further research shows that the number of equilibrium points can be determined by $4M+3$ and $4N+1$. In addition, for E_1 - E_4 , the corresponding

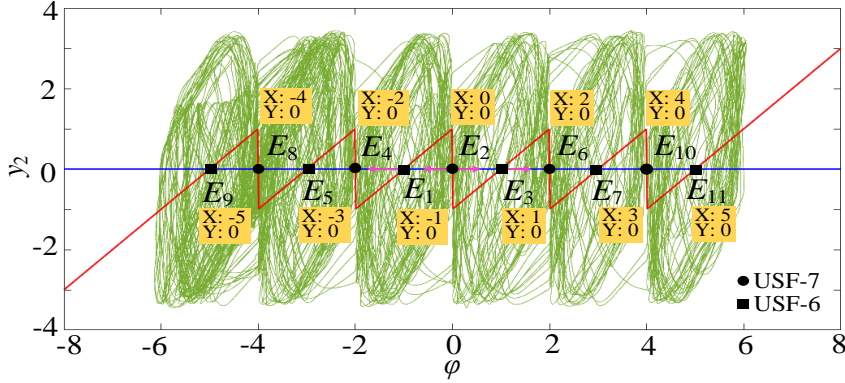


Figure 10: Hyperchaotic 6-structure attractor with eleven equilibria generated by $h_2(\varphi)$ with $M=2$.

Table 1
Equilibria, eigenvalues and stabilities

Equilibrium points	Eigenvalues	Stabilities
E1(0,0,0,0,0,0,-1)	(-1.2, -15.5582, 0.2266±8.8981j, 0.7548±3.0877j, 0.7277±1.8079j)	USF-6
E2(0,0,0,0,0,0,0)	(1199998.8, -15.7210, 0.2271±8.8979j, 0.7547±3.0878j, 0.7287±1.8068j)	USF-7
E3(0,0,0,0,0,0,1)	(-1.2, -15.8838, 0.2276±8.8977j, 0.7547±3.0880j, 0.7296±1.8058j)	USF-6
E4(0,0,0,0,0,0,-2)	(1199998.8, -15.3952, 0.2261±8.8983j, 0.7548±3.0876j, 0.7267±1.8089j)	USF-7

eigenvalues and stabilities are listed in Table 1. From Table 1, there exist two types of equilibria: unstable saddle-foci with index 6 (USF-6) and unstable saddle-foci with index 7 (USF-7). According to the Shil'nikov theorem, the MANN can generate self-excited chaos. As shown in Fig.10, the hyperchaotic attractor with six structures can be generated under this case. Particularly, the structures and bond orbits are yielded in the neighborhoods of USF-6 and USF-7 equilibrium points, respectively. That is to say, each USF-6 equilibrium point corresponds to a special structure. Thus six structures are generated in this situation, which is consistent with Fig.10. Therefore, the multi-pieces memristor synapse plays a crucial role in the generation of complex dynamics in the MANN.

4. Encryption application

To investigate the application of the MANN, this section designs a MANN-based color image encryption scheme, and the test results are analyzed.

4.1 Encryption scheme design

Hyperchaotic multi-structure attractors with multiple irregular attractor structures have flexible adjustability and high complexity, which makes them have a more promising application for information encryption. Here, based on the encryption method in [46], a new color image encryption scheme is designed by using the hyperchaotic 8-structure attractors generated by MANN. The encryption and decryption processes are described in the following steps.

Step 1: Set $a=1$, $b=0.01$, $c=2.2$, $d=1.2$, $\mu=8$, $M=3$ and initial states $(0.1, 0.1, 0.1, 0.1, 0.1, 0.1, 0.1, 0.1)$, discarded number $N_0=500$, and time step $\Delta t=0.001$, the MANN is continuously iterated to generate eight hyperchaotic 8-structure sequences $x_1(i)$, $x_2(i)$, $x_3(i)$, $x_4(i)$, $y_1(i)$, $y_2(i)$, $y_3(i)$, $\varphi(i)$. Note that the purpose of the hyperchaotic sequences is to produce random number. Thus, it is important to select suitable system parameters which can generate chaotic attractors.

Step 2: To obtain a pseudo-random sequence, the generated hyperchaotic multi-structure sequences are preprocessed as

$$\begin{cases} K_1(i) = x_1(i) + x_2(i) + x_3(i) + x_4(i) \\ K_2(i) = \text{mod}(\text{floor}((y_1(i) + y_2(i) + y_3(i) + \varphi(i)) * 10^{15}), 256) \end{cases} \quad (11)$$

Table 2

Encryption process with different images, steps of integration and initial conditions

Images	Step	Initial condition
Lena/Fig.11(a ₁)	0.001	(0.1, 0.1, 0.1, 0.1, 0.1, 0.1, 0.1, 0.1, 0.1)
Fruit/Fig.11(a ₂)	0.005	(0.1, 0, 0, 0.1, 0.1, 0, 0, 0.1)
House/Fig.11(a ₃)	0.01	0, 0, 0.1, 0.1, 0, 0, 0.1, 0.1)
Parrot/Fig.11(a ₄)	0.05	(0, 0.1, 0.1, 0, 0, 0.1, 0.1, 0)

where the floor(x) is the elements of x to the nearest integer less than or equal to x . It should be emphasized that to obtain a larger randomness, a trial and error method is adopted in this step. Numerous simulations show that the values of $K_1(i)$ and $K_2(i)$ have more large randomness under this case.

Step 3: Divide the original color image P into red P_r , green P_g , and blue P_b components.

Step 4: According to the index sequence, the three images P_r , P_g , and P_b are globally scrambled to be three sequences

$$\begin{cases} P_{r1}(i) = P_r(\text{index}(K_1(i))) \\ P_{g1}(i) = P_g(\text{index}(K_1(i))) \\ P_{b1}(i) = P_b(\text{index}(K_1(i))) \end{cases} \quad (12)$$

Step 5: The processed images are encrypted by means of XOR operation

$$\begin{cases} C_r(i) = P_{r1}(i) \oplus K_2(i) \\ C_g(i) = P_{g1}(i) \oplus K_2(i) \\ C_b(i) = P_{b1}(i) \oplus K_2(i) \end{cases} \quad (13)$$

until all elements are encrypted.

Step 6: Obtain the encrypted image C by combining C_r , C_g , and C_b .

Step 7: Decryption is the reverse process of the encryption operation.

4.2 Performance analysis

To demonstrate the efficiency of the designed image encryption scheme, four color images with the size of 512×512 are chosen as the encryption objects, as shown in Fig.11(a₁)-(a₄). It should be noted that the four original images are encrypted by selecting different steps of integration and initial conditions, as shown in Table 2. The experimental results and the security performance analyses including histogram, correlation coefficient, information entropy, key sensitivity, data loss, and noise attacks are presented in the following.

1) Histogram analysis: Histogram describes the distribution of pixel intensity in the image. A good encryption scheme should produce a uniform histogram. Fig.11 shows the original images, the encrypted images, and their respective histograms. Clearly, the encrypted images look cluttered and completely loses their original information. The histograms of the encrypted images are almost uniform, which means that it is difficult to get any useful statistical information from the encrypted images. Thus, the proposed image encryption scheme is enough to resist statistical attacks.

2) Correlation analysis: Correlation reflects the relationship between adjacent pixels in the image. Normally, Original images have a strong correlation in horizontal, vertical, and diagonal directions. The correlation coefficient can be computed by [59]

$$\rho_{xy} = \frac{\sum_{i=1}^N (x_i - E(x))(y_i - E(y))}{\sqrt{\sum_{i=1}^N (x_i - E(x))^2} \sqrt{\sum_{i=1}^N (y_i - E(y))^2}} \quad (14)$$

where x and y represent the intensity values of two adjacent pixels. To evaluate the correlation coefficients, 10000 pairs of pixels were randomly chosen in three directions from the original image "Lena" and the corresponding encrypted image. The obtained correlation coefficients of the original image are 0.9874, 0.9775, and 0.9720, respectively,

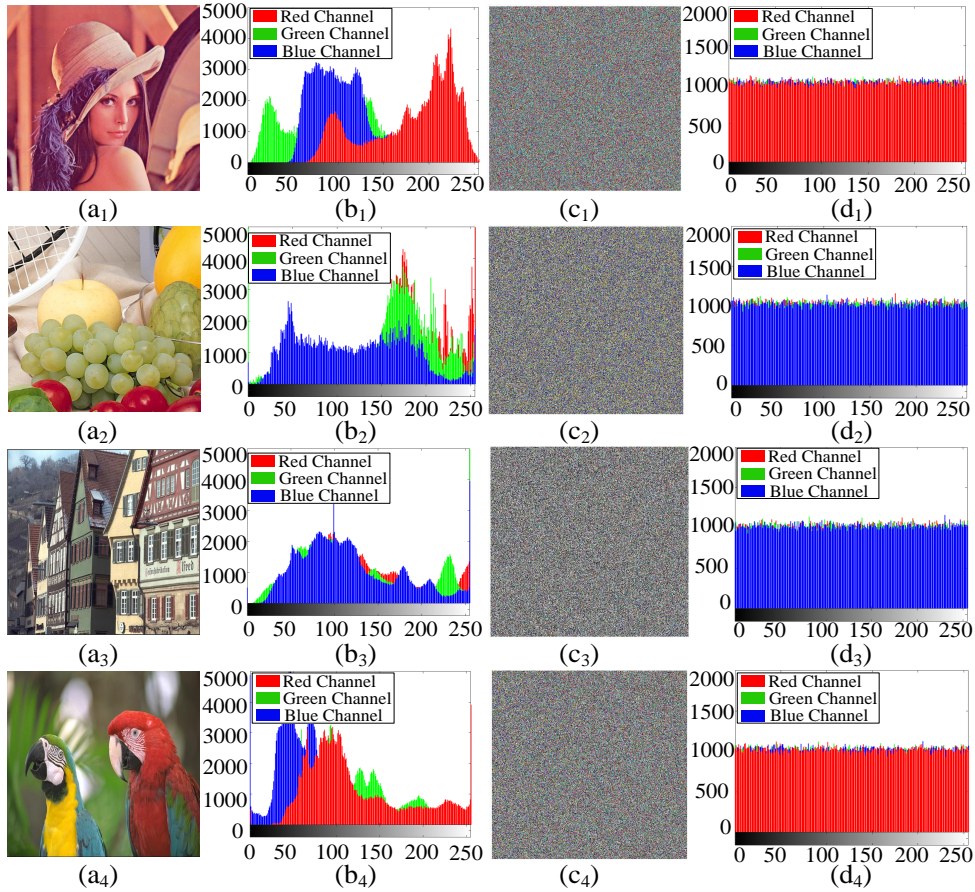


Figure 11: Encryption results. (a₁)-(a₄) original images. (b₁)-(b₄) histograms of the original images. (c₁)-(c₄) encrypted images. (d₁)-(d₄) histograms of the encrypted images.

Table 3

Correlation coefficients in different schemes

Refs	Images	Horizontal	Vertical	Diagonal
[33]	Lena 256*256	-0.00112	0.00091	0.00113
[34]	Lena 512*512	0.0058	0.0130	0.01343
[35]	Lena 512*512	0.00913	0.00643	0.00446
[36]	Lena 512*512	-0.00221	-0.00139	0.00041
[46]	Lena 256*256	-0.001358	-0.001120	0.0001251
This work	Lena 512*512	0.00094	-0.00082	0.00037

whereas the corresponding average values of the encrypted image are 0.00094, -0.00082, and 0.00037, respectively. There is no doubt that the proposed image encryption scheme can greatly reduce the correlation of the original images. Meanwhile, it can be seen from Table 3 that the image encrypted by the proposed encryption scheme has a lower correlation in three directions. Therefore, the designed cryptosystem owns great resistance to statistical attacks.

3) Entropy analysis: Information entropy reflects the randomness of image information. The information entropy is defined as [59]

$$H(P) = \sum_{i=0}^{2^N-1} P(x_i) \log_2 \frac{1}{P(x_i)} \quad (15)$$

Table 4
Information entropy in different schemes

Refs	RGB	Red	Green	Blue
[33]	7.9991	7.9972	7.9967	7.9985
[34]	7.9993	7.9993	7.9994	7.9993
[35]	7.9994	7.9994	7.9993	7.9993
[36]	7.9994	7.9994	7.9993	7.9993
[46]	7.9977	--	--	--
This work	7.9998	7.9994	7.9994	7.9994

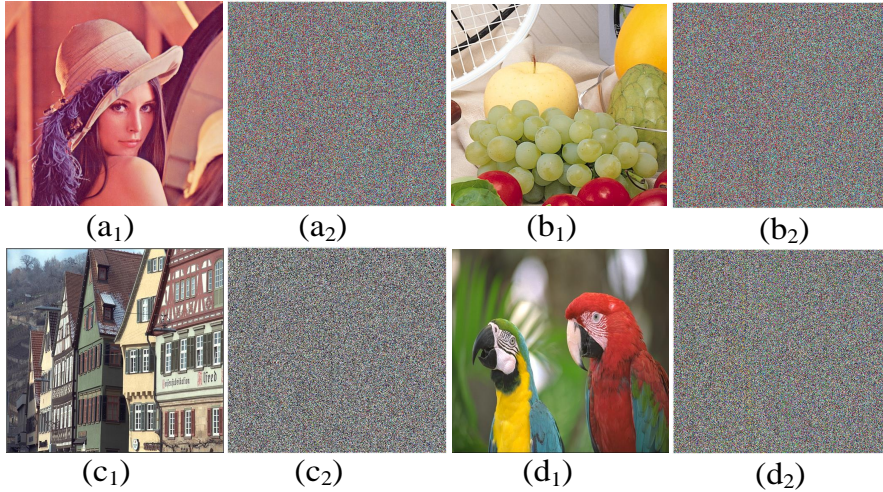


Figure 12: Test results for key sensitivity. (a₁)-(d₁) Accurate decrypted images with right secret key. (a₂)-(d₂) Inaccurate decrypted images with the tiny change (10^{-16}) of the secret key.

Table 5
Key sensitivity in different schemes

Refs	[33]	[34]	[35]	[36]	[46]	This work
Key sensitivity	10^{-14}	10^{-14}	10^{-14}	--	10^{-15}	10^{-16}

where $P(x_i)$ denotes the probability of x_i and N represents the number of the information source. The maximum theoretical information entropy is 8. Table 4 gives the calculation results of information entropy under different channels. From the results in Table 4, the information entropy of the presented scheme is closer to the theoretical value compared with other similar schemes.

4) Sensitivity analysis: Key sensitivity is a key measure of the security of encryption algorithms. Good image encryption schemes should be key-sensitive. The initial values ($x_{10}, x_{20}, x_{30}, x_{40}, y_{10}, y_{20}, y_{30}, \varphi_0$) are used as secret keys in this encryption scheme. The decrypted images are shown in Fig.12(a₁)-(d₁) with the right secret key. With a slight change of the secret key, Fig.12(a₂)-(d₂) illustrates the wrong decrypted images. Despite the fact that the secret key has been changed a little (10^{-16}), the decrypted images are completely different from the original images. As shown in Table 5, compared with other similar image encryption schemes, the proposed image encryption scheme has higher sensitivity to the key.

5) Attack analysis: Image data is susceptible to data loss and noise attacks during transmission. We first cut off some parts of the encrypted images and then decrypt them. As shown in Fig.13, data loss attack for the different lost areas are successfully decrypted for the original image to be recovered. Besides, salt and pepper noise with different densities are added to the encrypted images and then decrypt them. It can be seen from Fig.13 that some pixel values

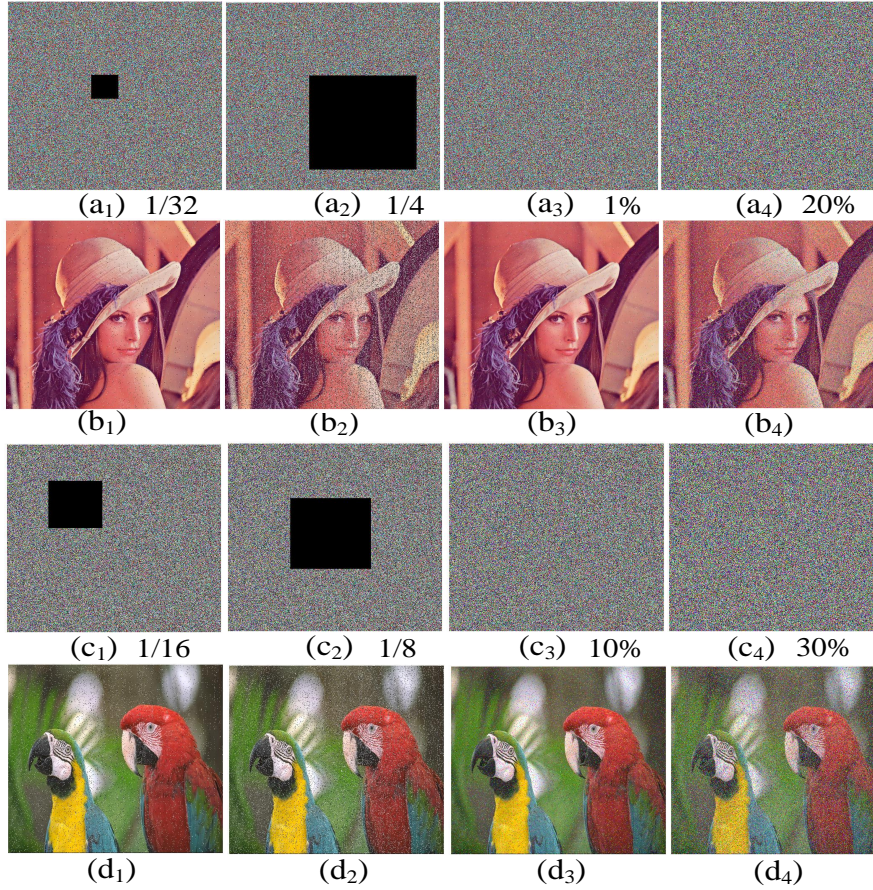


Figure 13: Test results for data loss and noise attacks. (a₁), (a₂), (c₁), and (c₂) the encrypted images with 1/32, 1/4, 1/16, and 1/8 loss, respectively. (b₁), (b₂), (d₁), and (d₂) corresponding decrypted images. (a₃), (a₄), (c₃), and (c₄) the encrypted images with 1%, 20%, 10%, and 30% salt and pepper noise, respectively. (b₃), (b₄), (d₃), and (d₄) corresponding decrypted images.

Table 6
Attack resistance in different schemes

Refs	[33]	[35]	[36]	[37]	This work
Attack resistance	No	No	No	No	Yes

in the decrypted images have been changed, however, the approximate information of the original image can still be recovered successfully. Compared with other schemes in Table 6, the proposed encryption scheme is able to withstand data loss and noise attacks. So it has higher security.

6) SSIM analysis: Structural similarity (SSIM) represents the similarity between two different images. For two images x and y , SSIM can be expressed as follows [60]

$$SSIM(x, y) = \frac{(2\mu_x\mu_y + c_1)(2\sigma_{xy} + c_2)}{(\mu_x^2 + \mu_y^2 + c_1)(\sigma_x^2 + \sigma_y^2 + c_2)} \quad (16)$$

where μ_x and μ_y are average values, σ_x^2 and σ_y^2 are variance, and σ_{xy} is the covariance. $c_1 = (k_1L)^2$ and $c_2 = (k_2L)^2$ are two constants, where $k_1=0.01$, $k_2=0.03$, and L is the dynamic range of pixel values. Table 7 gives the results of SSIM for all the encrypted images and decrypted images compared with the original image. It can be seen from Table 6 that the SSIM value of the encrypted image in Fig.11(c₁) is close to the ideal value of 0, and the accurate

Table 7
SSIM values for different images

Images	SSIM(R)	SSIM(G)	SSIM(B)
Fig.11(c ₁)	0.0082	0.0073	0.0090
Fig.12(a ₁)	1	1	1
Fig.12(a ₂)	0.0052	0.0168	0.0128
Fig.12(b ₂)	0.0073	0.0174	0.0140
Fig.13(b ₁)	0.8703	0.9031	0.8319
Fig.13(b ₂)	0.5852	0.6523	0.5042
Fig.13(b ₃)	0.9785	0.9840	0.9714
Fig.13(b ₄)	0.6565	0.7152	0.5754

decrypted image in Fig.12(a₁) has an ideal SSIM value of 1. The test results mean that the encryption scheme has a good encryption effect. Moreover, the inaccurate decrypted images in Fig.12(a₂) and Fig.12(b₂) exhibit very low values of SSIM, which means that the encryption scheme has a high key sensitivity. On the contrary, under noise and data loss attacks, the decrypted images in Fig.13(b₁)-(b₂) and Fig.13(b₃)-(b₄) exhibit high values of SSIM, which shows that the main image information can be well recovered when the original images suffered from data loss and noise attacks.

From the aforementioned performance analyses, it can be concluded that the proposed image encryption scheme has some advantages in terms of correlation, information entropy, and key sensitivity. Additionally, it has strong abilities to resist statistical attacks and noise and data loss attacks. Although [46] reported an encryption scheme based on the multi-structure attractors, the proposed hyperchaotic multi-structure attractors have more advantages including high-security performance and good encryption effect in chaos-based image encryption application and are worthy of further discussion and promotion.

5. Circuit implementation and verification

Circuit implementation is often used to experimental study the dynamical behaviors of some nonlinear systems. To further verify the dynamic characteristics of the MANN, this section designs the analog circuit of the MANN, and the numerical simulations are verified by Multisim simulations and hardware experiments.

5.1 Circuit design

The circuit of MANN is implemented by adopting a module-based unified circuit realization method [20]. Due to the lack of technical measures, the nano-memristor devices have not yet been commercialized [61]. Thus, an equivalent circuit in [46] to realize the multi-pieewise memristor is used in this paper, as shown in Fig.14(b). Before designing a MANN circuit, a negative hyperbolic tangent function circuit is introduced from [8], as shown in Fig.14(a). It should be pointed out that the memristors with different values of control parameters N/M can be realized by selecting different bias voltages (e_i) and switches (W_i). According to (6), the circuit structure of the MANN is designed as shown in Fig.15. Here, seven membrane potentials $x_1, x_2, x_3, x_4, y_1, y_2,$ and y_3 are emulated by seven output voltages $v_{x1}, v_{x2}, v_{x3}, v_{x4}, v_{y1}, v_{y2}, v_{y3}$, respectively. All synaptic weight coefficients are simulated by the resistors R_{x1} - R_{x14} and R_{y1} - R_{y8} . Based on the circuit in Fig.15, the circuit state equations can be described by

$$\begin{cases} RC\dot{v}_{x1} = -v_{x1} + \frac{R}{R_{x1}} \tanh(v_{x1}) + \frac{R}{R_{x2}} \tanh(v_{x2}) - \frac{R}{R_{x3}} \tanh(v_{x3}) - \frac{R}{R_{x4}} \tanh(v_{x4}) - \left(\frac{R}{R_a} + \frac{gRv_\varphi}{R_b} \right) (v_{x1} - v_{y1}) \\ RC\dot{v}_{x2} = -v_{x2} + \frac{R}{R_{x5}} \tanh(v_{x2}) + \frac{R}{R_{x6}} \tanh(v_{x3}) - \frac{R}{R_{x7}} \tanh(v_{x4}) \\ RC\dot{v}_{x3} = -v_{x3} + \frac{R}{R_{x8}} \tanh(v_{x1}) - \frac{R}{R_{x9}} \tanh(v_{x2}) + \frac{R}{R_{x10}} \tanh(v_{x3}) + \frac{R}{R_{x11}} \tanh(v_{x4}) \\ RC\dot{v}_{x4} = -v_{x4} + \frac{R}{R_{x12}} \tanh(v_{x1}) + \frac{R}{R_{x13}} \tanh(v_{x3}) + \frac{R}{R_{x14}} \tanh(v_{x4}) \\ RC\dot{v}_{y1} = -v_{y1} + \frac{R}{R_{y1}} \tanh(v_{y1}) + \frac{R}{R_{y2}} \tanh(v_{y2}) - \frac{R}{R_{y3}} \tanh(v_{y3}) + \left(\frac{R}{R_a} + \frac{gRv_\varphi}{R_b} \right) (v_{x1} - v_{y1}) \\ RC\dot{v}_{y2} = -v_{y2} + \frac{R}{R_{y4}} \tanh(v_{y2}) + \frac{R}{R_{y5}} \tanh(v_{y3}) \\ RC\dot{v}_{y3} = -v_{y3} + \frac{R}{R_{y6}} \tanh(v_{y1}) - \frac{R}{R_{y7}} \tanh(v_{y2}) + \frac{R}{R_{y8}} \tanh(v_{y3}) \\ RC\dot{v}_\varphi = \frac{R}{R_c} (v_{x1} - v_{y1}) - \frac{R}{R_d} h(v_\varphi) \end{cases} \quad (17)$$

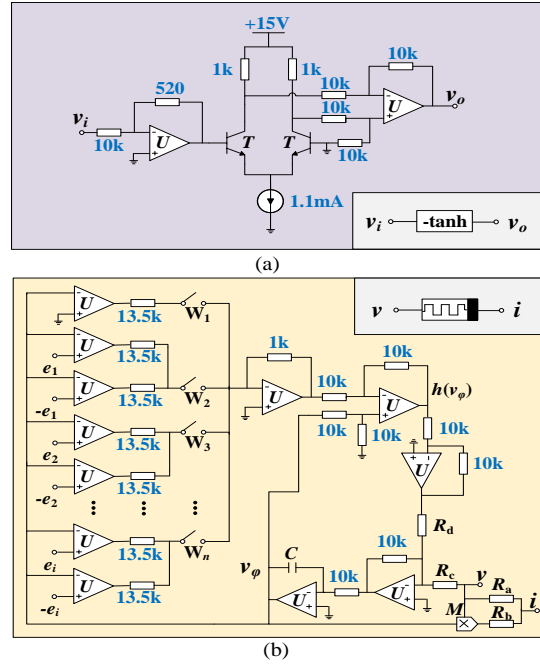


Figure 14: Circuit structure. (a) negative hyperbolic tangent function circuit. (b) multi-pieewise memristor circuit.

Let $C_{x1}=C_{x2}=C_{x3}=C_{x4}=C_{y1}=C_{y2}=C_{y3}=C$, $RC=100\mu s$, $R=10k\Omega$ and $C=10nF$. Considering the fixed synaptic weight coefficients, corresponding resistances can be calculated as $R_{x1}=5.55k\Omega$, $R_{x2}=2.98k\Omega$, $R_{x3}=20k\Omega$, $R_{x4}=0.83k\Omega$, $R_{x5}=10k\Omega$, $R_{x6}=0.5k\Omega$, $R_{x7}=20k\Omega$, $R_{x8}=20k\Omega$, $R_{x9}=2.5k\Omega$, $R_{x10}=5.5k\Omega$, $R_{x11}=2.5k\Omega$, $R_{x12}=12.19k\Omega$, $R_{x13}=20k\Omega$, $R_{x14}=5k\Omega$. $R_{y1}=100k\Omega$, $R_{y2}=20k\Omega$, $R_{y3}=4k\Omega$, $R_{y4}=3.33k\Omega$, $R_{y5}=3.33k\Omega$, $R_{y6}=10k\Omega$, $R_{y7}=3.33k\Omega$, $R_{y8}=10k\Omega$. Besides, for the memristor circuit, $R_a=R/\mu a$, $R_b=R/\mu b$, $R_c=R/c$ and $R_d=R/d$.

5.2 Multisim simulation and hardware experiment

The designed MANN circuit is simulated on the Multisim 14.0 platform with $M/AD633JN$, $U/TL082CP$, $T/MPS2222$, and $\pm 15V$ DC voltage supplies. Numerous experiments show that the designed MANN circuit can generate results consistent with the numerical simulation results in section 3. For example, when all switches are open, letting $R_c=4.52k\Omega$ ($c=2.2$) and $R_d=8.8k\Omega$ ($d=1.2$), setting initial capacitor voltages (0.1V, 0.1V, 0.1V, 0.1V, 0.1V, 0.1V, 0.1V, 0.1V), and selecting different values of R_a and R_b , the hyperchaotic attractors with amplitude control can be captured as shown in Fig.16. Now we set $R_a=1.31k\Omega$ ($a=1, \mu=8$), $R_b=13.1k\Omega$ ($b=0.01, \mu=8$), $R_c=20k$ ($c=0.5$) and $R_d=8.8k\Omega$ ($d=1.2$). The initial voltage of the memristor circuit is chosen as v_φ V, where $v_\varphi=-7, -5, -3, -1, 1, 3, 5$, and 7 . When W_1, W_2, W_3 , and W_4 are off, set $e_1=2V$, $e_2=4V$, and $e_3=6V$. The simulation results for these settings are given in Fig.17. As the MANN circuit generates hyperchaotic initial-boosted behavior with coexisting eight hyperchaotic attractors under different initial capacitor voltages. Besides, when keeping the resistances unchanged except for $R_c=4.52k\Omega$ ($c=2.2$) and all initial capacitor voltages 0.1V, hyperchaotic multi-structure attractors can be captured by selecting different control switches and voltages, as shown in Fig.18. Obviously, the circuit simulation results in Fig.18 are consistent well with the numerical simulation results in Fig.7. It is noted that compared with numerical simulations, the resistances of some resistors exist some difference due to the circuit's parasitic parameters, which can be solved by fine-tuning the adjustable resistors.

In addition, based on the circuit diagram in Fig.14 and Fig.15, a hardware circuit is physically implemented by using discrete active and passive electronic components, as shown in Fig.19(a). The circuit parameters are the same as the Multisim simulation. The obtained hyperchaotic 3-structure and 4-structure chaotic attractors observed by the oscilloscope GWINSTED GDS-1102-AU are shown in Fig.19(b) and Fig.19(c), respectively. Obviously, the experimental results match those obtained from the numerical simulations and circuit simulations. Through the circuit experiment,

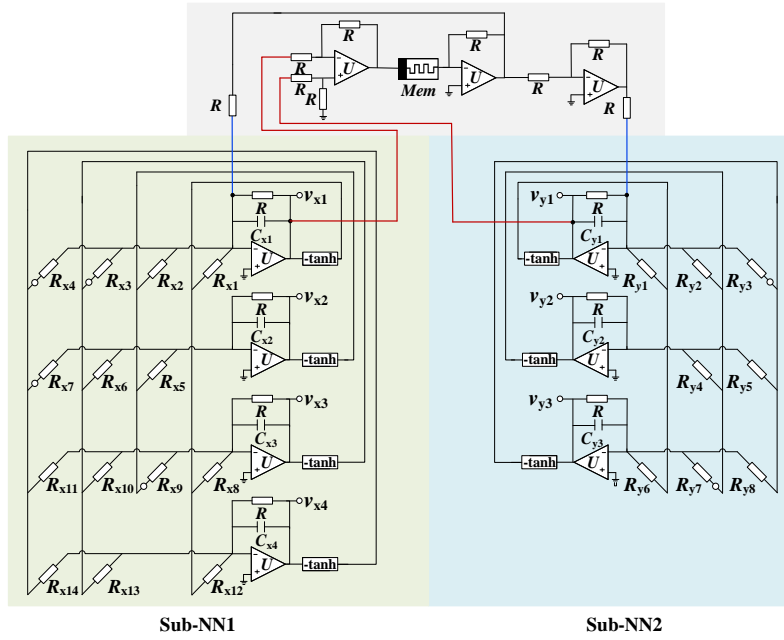


Figure 15: MACNN circuit structure.

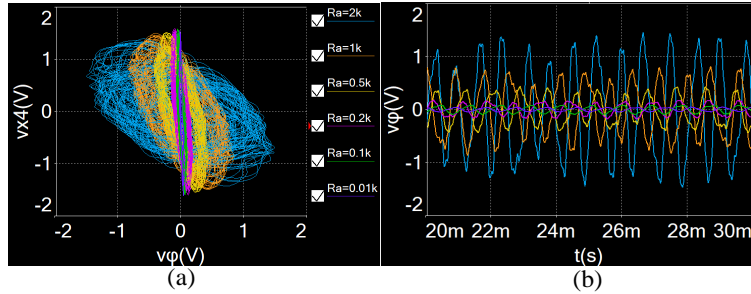


Figure 16: Circuit experimental results of Hyperchaos with amplitude control. (a) Hyperchaotic attractor with $(R_a, R_b) = (2k\Omega, 20k\Omega), (1k\Omega, 10k\Omega), (0.5k\Omega, 5k\Omega), (200\Omega, 2k\Omega), (100\Omega, 1k\Omega), (10\Omega, 100\Omega)$. (b) Generating voltage signals v_φ .

it concludes that the MANN can be physically realized and can be further applied to explore practical applications.

6. Conclusion

In this paper, a new memristor-coupled asymmetric neural network model is proposed and investigated. The dynamic characteristics related to parameters, initial states, and equilibrium points of the model are analyzed. Research has revealed that the proposed MANN can exhibit some complex chaotic dynamics including infinitely wide hyperchaos with amplitude control, hyperchaotic initial-boosted behavior, and the arbitrary number of hyperchaotic multi-structure attractors. Especially, the dynamic phenomena of the infinitely wide hyperchaos and the hyperchaotic multi-structure attractors are observed in neural networks for the first time. It has also been found that the memristor synapse plays a key role in the dynamic characteristics of the presented MANN. The positions of the hyperchaotic attractors and the number of hyperchaotic multi-structure attractors can be controlled respectively by initial values and parameters of the memristor synapse. Moreover, to investigate the application of the MANN, a color image encryption scheme based on the MANN is proposed. Experimental results demonstrate that compared with similar schemes the designed

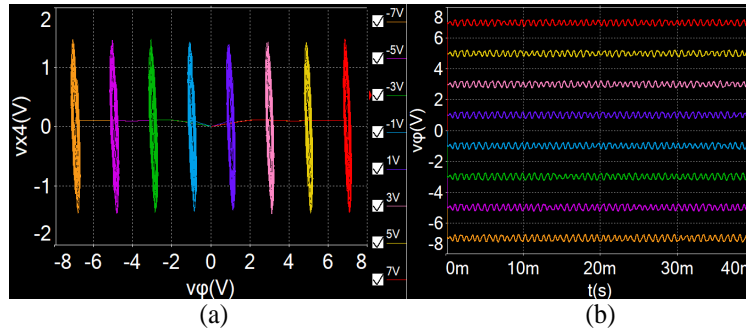


Figure 17: Circuit experimental results of hyperchaotic initial-boosted behavior. (a) Phase portraits. (b) Signal waveform.

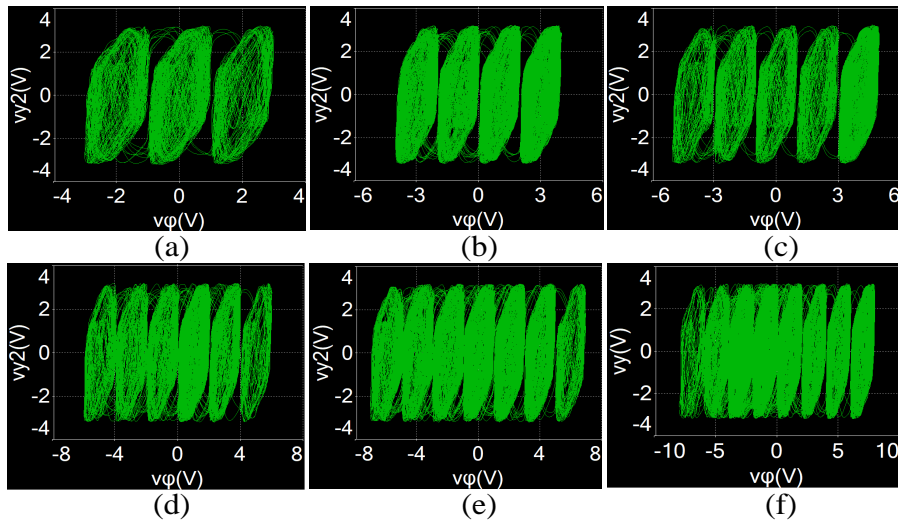


Figure 18: Circuit experimental results of Hyperchaotic multi-structure attractors. (a) 3-structure. (b) 4-structure. (c) 5-structure. (d) 6-structure. (e) 7-structure. (f) 8-structure.

encryption scheme has higher security. Finally, the hardware circuit of the MANN is implemented, and various complex dynamical phenomena are further verified. Modeling, analysis, simulation, and circuit realization of the neural network as attempted in this article would be helpful for artificial intelligence. However, how to apply the MANN to practical scenarios remains to be further investigated.

Declaration of Competing Interest

The authors declare that they have no potential conflict of interest.

Acknowledgments

This work is supported by the National Natural Science Foundation of China (62201204, 62171182, 61971185), the China Postdoctoral Science Foundation (2022M711104, 2020M682552), and the Natural Science Foundation of Hunan Province (2021JJ3014).

References

- [1] S. J. Schiff, K. Jerger, D. H. Duong, et al, "Controlling chaos in the brain," *Nature.*, vol. 370, no. 6491, pp. 615-620, 1994.

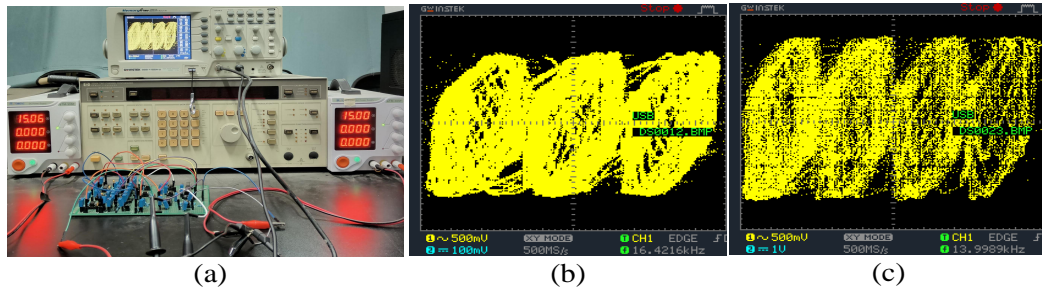


Figure 19: Experiment results of hyperchaotic multi-structure attractors. (a) Hardware experiment platform. (b) 3-structure attractor. (c) 4-structure attractor.

- [2] F. Yu, H. Shen, Z. Zhang, et al. "Dynamics analysis, hardware implementation and engineering applications of novel multi-style attractors in a neural network under electromagnetic radiation," *Chaos Solitons Fractals.*, vol. 152, p. 111350, 2021.
- [3] Z. Hou, J. Ma, X. Zhan, et al. "Estimate the electrical activity in a neuron under depolarization field," *Chaos Solitons Fractals.*, vol. 142, p. 110522, 2021.
- [4] J. J. Hopfield, "Neurons with graded response have collective computational properties like those of two-state neurons," *Proc. Nat. Acad. Sci. USA.*, vol. 81, no. 10, pp. 3088-3092, 1984.
- [5] X. S. Yang, Q. Yuan. "Chaos and transient chaos in simple Hopfield neural networks," *Neurocomputing.*, vol. 69, no. 1-3, pp. 232-241, 2005.
- [6] Y. Huang, X. S. Yang. "Hyperchaos and bifurcation in a new class of four-dimensional Hopfield neural networks," *Neurocomputing.*, vol. 69, no. 13-15, pp. 1787-1795, 2006.
- [7] H. Lin, C. Wang, C. Chen, et al. "Neural bursting and synchronization emulated by neural networks and circuits," *IEEE Trans. Circuits Syst. I-Regul. Pap.*, vol. 68, no. 8, pp. 3397-3410, 2021.
- [8] B. Bao, H. Qian, J. Wang, et al. "Numerical analyses and experimental validations of coexisting multiple attractors in Hopfield neural network," *Nonlinear Dyn.*, vol. 90, no. 4, pp. 2359-2369, 2017.
- [9] D. B. Strukov, G. S. Snider, D. R. Stewart, et al. "The missing memristor found," *Nature.*, vol. 453, pp. 80-83, 2008.
- [10] F. Wu, H. Gu, Y. Jia, et al. "Bifurcations underlying different excitability transitions modulated by excitatory and inhibitory memristor and chemical autapses," *Chaos Solitons Fractals.*, vol. 153, p. 111611, 2021.
- [11] D. Ding, X. Chen, Z. Yang, et al. "Coexisting multiple firing behaviors of fractional-order memristor-coupled HR neuron considering synaptic crosstalk and its ARM-based implementation," *Chaos Solitons Fractals.*, vol. 158, p. 112014, 2022.
- [12] D. V. Guseinov, A. N. Mikhaylov, Y. V. Pershin. "The rich dynamics of memristive devices with non-separable nonlinear response." *IEEE Trans. Circuits Syst. II-Express Briefs.*, vol. 69, no. 3, pp. 1802-1806, 2021.
- [13] D. V. Guseinov, I. V. Matyushkin, N. V. Chernyaev, et al. "Capacitive effects can make memristors chaotic." *Chaos Solitons Fractals.*, vol. 144, p. 110699, 2021.
- [14] C. Pan, Q. Hong, X. Wang. "A novel memristive chaotic neuron circuit and its application in chaotic neural networks for associative memory," *IEEE Trans. Comput-Aided Des. Integr. Circuits Syst.*, vol. 40, no. 3, pp. 521-532, 2021.
- [15] R. Wang, C. Li, S. Kong, et al. "A 3D memristive chaotic system with conditional symmetry," *Chaos Solitons Fractals.*, vol. 158, p. 111992, 2022.
- [16] Z. T. Njitacke, C. N. Takembo, J. Awrejcewicz, et al. "Hamilton energy, complex dynamical analysis and information patterns of a new memristive FitzHugh-Nagumo neural network," *Chaos Solitons Fractals.*, vol. 160, p. 112211, 2022.
- [17] C. Chen, J. Chen, H. Bao, et al. "Coexisting multi-stable patterns in memristor synapse-coupled Hopfield neural network with two neurons," *Nonlinear Dyn.*, vol. 95, no. 4, pp. 3385-3399, 2019.
- [18] H. Lin, C. Wang, Q. Hong, et al. "A multi-stable memristor and its application in a neural network," *IEEE Trans. Cir. Sys.-II: Brief Papers.*, vol. 67, no. 12, pp. 3472-3476, 2020.
- [19] I. S. Doubla, B. Ramakrishnan, Z. T. Njitacke, et al. "Hidden extreme multistability and its control with selection of a desired attractor in a non-autonomous Hopfield neuron," *AEU-Int. J. Electron. Commun.*, vol. 144, p. 154059, 2022.
- [20] S. Zhang, J. Zheng, X. Wang, et al. "Initial offset boosting coexisting attractors in memristive multi-double-scroll Hopfield neural network," *Nonlinear Dyn.*, vol. 102, no. 4, pp. 2821-2841, 2020.
- [21] H. Lin, C. Wang, L. Cui, et al. "Brain-like initial-boosted hyperchaos and application in biomedical image encryption," *IEEE Trans. Ind. Informat.*, vol. 18, no. 12, pp. 8839-8850, 2022.
- [22] M. Ignatov, M. Ziegler, M. Hansen, et al. "Memristive stochastic plasticity enables mimicking of neural synchrony: Memristive circuit emulates an optical illusion." *Sci. Adv.*, vol. 3, no. 10, p. e1700849, 2017.

- [23] S. A. Gerasimova, A. I. Belov, D. S. Korolev, et al. "Stochastic memristive interface for neural signal processing." *Sensors.*, vol. 21, no. 16, p. 5587, 2021.
- [24] M. A. Mishchenko, D. I. Bolshakov, V. I. Lukoyanov, et al. "Inverted spike-rate-dependent plasticity due to charge traps in a metal-oxide memristive device." *J. Phys. D-Appl. Phys.*, vol. 55, no. 39, p. 394002, 2022.
- [25] S. G. Hu, Y. Liu, Z. Liu, et al. "Associative memory realized by a reconfigurable memristive Hopfield neural network." *Nat. Commun.*, vol. 6, no. 1, p. 7522, 2015.
- [26] Z. Fahimi, M. R. Mahmoodi, H. Nili, et al. "Combinatorial optimization by weight annealing in memristive hopfield networks." *Sci Rep.*, vol. 11, no. 1, p. 16383, 2021.
- [27] O. Krestinskaya, K. N. Salama, and A. P. James, "Learning in memristive neural network architectures using analog backpropagation circuits," *IEEE Trans. Circuits Syst. I, Reg. Papers.*, vol. 66, no. 2, pp. 719-732, 2019.
- [28] J. Sun, X. Xiao, Q. Yang, et al. "Memristor-based Hopfield network circuit for recognition and sequencing application," *AEU Int. J. Electron. Commun.*, vol. 134, p. 153698, 2021.
- [29] S. Xu, X. Wang, X. Ye. "A new fractional-order chaos system of Hopfield neural network and its application in image encryption," *Chaos Solitons Fractals.*, vol. 157, p. 111889, 2022.
- [30] X. Wang, N. Guan, J. Yang. "Image encryption algorithm with random scrambling based on one-dimensional logistic self-embedding chaotic map," *Chaos Solitons Fractals.*, vol. 150, p. 111117, 2021.
- [31] H. Bao, Z. Hua, H. Li, et al. "Memristor-based hyperchaotic maps and application in auxiliary classifier generative adversarial nets," *IEEE Trans. Ind. Informat.*, vol. 18, no. 8, pp. 5297-5306, 2022.
- [32] Q. Lai, C. Lai, H. Zhang, et al. "Hidden coexisting hyperchaos of new memristive neuron model and its application in image encryption," *Chaos Solitons Fractals.*, vol. 158, p. 112017, 2022.
- [33] N. Bigdeli, Y. Farid, K. Afshar. "A robust hybrid method for image encryption based on Hopfield neural network," *Comput. Electr. Eng.*, vol. 38, no. 2, pp. 356-369, 2012.
- [34] X. Y. Wang, Z. M. Li. "A color image encryption algorithm based on Hopfield chaotic neural network," *Opt. Lasers Eng.*, vol. 115, pp. 107-118, 2019.
- [35] L. Liu, L. Zhang, D. Jiang, et al. "A simultaneous scrambling and diffusion color image encryption algorithm based on Hopfield chaotic neural network," *IEEE Access.*, vol. 7, pp. 185796-185810, 2019.
- [36] E. Tlelo-Cuautle, J. D. Díaz-Muñoz, A. M. González-Zapata, et al. "Chaotic image encryption using hopfield and hindmarsh-rose neurons implemented on FPGA," *Sensors.*, vol. 20, no. 5, p. 1326, 2020.
- [37] Z. T. Njitacke, S. D. Isaac, T. Nestor, et al. "Window of multistability and its control in a simple 3D Hopfield neural network: application to biomedical image encryption," *Neural Comput. Appl.*, vol. 33, no. 12, pp. 6733-6752, 2021.
- [38] Q. Lai, Z. Wan, H. Zhang, et al. "Design and analysis of multiscroll memristive hopfield neural network with adjustable memductance and application to image encryption," *IEEE Trans. Neural Netw. Learn. Syst.*, DOI: 10.1109/TNNLS.2022.3146570, 2022.
- [39] A. Pascual, K. L. Huang, J. Neveu, et al. "Brain asymmetry and long-term memory," *Nature.*, vol. 427, no. 6975, pp. 605-606, 2004.
- [40] Z. B. Xu, G. Q. Hu, C. P. Kwong. "Asymmetric Hopfield-type networks: theory and applications." *Neural Net.*, vol. 9, no. 3, pp. 483-501, 1996.
- [41] P. Zheng, W. Tang, J. Zhang. "Efficient continuous-time asymmetric Hopfield networks for memory retrieval." *Neural Comput.*, vol. 22, no. 6, pp. 1597-1614, 2010.
- [42] D. Fasoli, A. Cattani, S. Panzeri. "Pattern storage, bifurcations, and groupwise correlation structure of an exactly solvable asymmetric neural network model." *Neural Comput.*, vol. 30, no. 5, pp. 1258-1295, 2018.
- [43] M. Breakspear. "Dynamic models of large-scale brain activity," *Nat. Neurosci.*, vol. 20, no. 3, pp. 340-352, 2017.
- [44] Q. K. Telesford, S. L. Simpson, J. H. Burdette, et al. "The brain as a complex system: using network science as a tool for understanding the brain," *Brain Connectivity.*, vol. 1, no. 4, pp. 295-308, 2011.
- [45] H. Lin, C. Wang, Q. Deng, et al. "Review on chaotic dynamics of memristive neuron and neural network," *Nonlinear Dyn.*, vol. 106, no. 1, pp. 959-973, 2021.
- [46] H. Lin, C. Wang, C. Xu, et al. "A memristive synapse control method to generate diversified multi-structure chaotic attractors," *IEEE Trans. Comput-Aided Des. Integr. Circuits Syst.*, DOI: 10.1109/TCAD.2022.3186516, 2022.
- [47] S. H. Jo, T. Chang, I. Ebong, et al. "Nanoscale memristor device as synapse in neuromorphic systems." *Nano letters.*, vol. 10, no. 4, pp. 1297-1301, 2010.
- [48] L. O. Chua. "Memristor, Hodgkin-Huxley, and edge of chaos." *Nanotechnology.*, vol. 24, no. 38, pp. 1-14, 2013.
- [49] P. Jin, G. Wang, H. H. C. Iu, et al. "A locally active memristor and its application in a chaotic circuit," *IEEE Trans. Cir. Sys.-II: Brief Papers.*, vol. 65, no. 2, pp. 246-250, 2018.
- [50] S. Rosemann, C. M. Thiel, "Audio-visual speech processing in age-related hearing loss: stronger integration and increased frontal lobe recruitment," *Neuroimage.*, vol. 175, pp. 425-437, 2018.
- [51] I. C. Mundinano, J. Chen, M. de Souza, et al. "More than blindsight: Case report of a child with extraordinary visual capacity following perinatal bilateral occipital lobe injury," *Neuropsychologia.*, vol. 128, pp. 178-186, 2019.

- [52] N. V. Stankevich, A. P. Kuznetsov, E. P. Seleznev. "Chaos and hyperchaos arising from the destruction of multifrequency tori," *Chaos Solitons Fractals.*, vol. 147, p. 110998, 2021.
- [53] J. V. N. Tegnitsap, H. B. Fotsin. "Multistability, transient chaos and hyperchaos, synchronization, and chimera states in wireless magnetically coupled VDPCL oscillators," *Chaos Solitons Fractals.*, vol. 158, p. 112056, 2022.
- [54] H. Lin, C. Wang, L. Cui, et al. "Hyperchaotic memristive ring neural network and application in medical image encryption," *Nonlinear Dyn.*, vol. 110, no. 01, pp. 841-855, 2022.
- [55] Y. Jiang, C. Li, C. Zhang, et al. "A double-memristor hyperchaotic oscillator with complete amplitude control," *IEEE Trans. Circuits Syst. I-Regul. Pap.*, vol. 68, no. 12, pp. 4935-4944, 2021.
- [56] M. Chen, X. Ren, H. Wu, et al. "Interpreting initial offset boosting via reconstitution in integral domain," *Chaos Solitons Fractals.*, vol. 131, p. 109544, 2020.
- [57] S. Gu, S. He, H. Wang, et al. "Analysis of three types of initial offset-boosting behavior for a new fractional-order dynamical system," *Chaos Solitons Fractals.*, vol. 143, p. 110613, 2021.
- [58] H. Lin, C. Wang, F. Yu, et al. "An extremely simple multiwing chaotic system: Dynamics analysis, encryption application, and hardware implementation," *IEEE Trans. Ind. Electron.*, vol. 68, no. 12, pp. 12708-12719, 2021.
- [59] A. Azam, M. Aqeel, D. A. Sunny. "Generation of multidirectional mirror symmetric multiscroll chaotic attractors (MSMCA) in double wing satellite chaotic system," *Chaos Solitons Fractals.*, vol. 155, p. 111715, 2022.
- [60] Z. Wang, A. C. Bovik, H. R. Sheikh, et al. "Image quality assessment: from error visibility to structural similarity." *IEEE Trans. Image Process.*, vol. 13, no. 4, pp. 600-612, 2004.
- [61] Y. Li, Z. Wang, R. Midya, et al. "Review of memristor devices in neuromorphic computing: materials sciences and device challenges." *J Phys D Appl Phys.*, vol. 51, no. 50, p. 503002, 2018.